processes

MDPI

Article

Bearing Fault Diagnosis Method Based on Multi-Domain Feature Selection and the Fuzzy Broad Learning System

Le Wu [1,2], Chao Zhang [1,2,*], Feifan Qin [1,2], Hongbo Fei [1,2], Guiyi Liu [1,2], Jing Zhang [1,2] and Shuai Xu [1,2]

[1] School of Mechanical Engineering, Inner Mongolia University of Science and Technology, Baotou 014010, China
[2] Inner Mongolia Key Laboratory of Intelligent Diagnosis and Control of Mechatronic System, Baotou 014010, China
* Correspondence: zhanghero123@163.com; Tel.: +86-138-4820-8042

Abstract: In recent years, the Broad Learning System (BLS) has been acknowledged for its potential to revolutionize traditional artificial intelligence methods due to its short training time, strong interpretability, and simple structure. In the evolution of BLS, Prof. C. L. Philip Chen's team introduced the Fuzzy Broad Learning System (FBLS) by replacing the feature nodes of BLS with fuzzy subsystems, thereby further reducing the training time. However, the traditional FBLS, with its straightforward structure, falls short in achieving higher fault diagnosis accuracy when handling raw vibration signals. This paper presents a bearing fault diagnosis approach employing multi-domain feature selection and the fuzzy broad learning system (MS-FBLS), aiming to enhance the diagnostic accuracy of FBLS through multi-domain feature selection. Primarily, a set of 49 features spanning time domain, frequency domain, time-frequency domain, and entropy values is extracted from the original vibrational signals. This combination builds a 49-dimensional multidomain feature set that exploits the information behind the input data as much as possible, thus compensating for the lack of feature extraction capability in FBLS. Afterward, the Random Forest algorithm assesses the significance of all features, leading to a reordering of the multidomain feature set based on their respective importance levels. Ultimately, the reorganized multidomain feature set is then fed into the FBLS, enabling the identification of various failure states within the bearing. The experimental validation conducted on the rolling bearing fault simulation test bed showcased that, in comparison to the traditional FBLS, the MS-FBLS method not only elevates diagnostic accuracy by 23.46%, but also substantially enhances diagnostic speed. These results serve as comprehensive evidence affirming the effectiveness of the method.

Keywords: multi-domain feature extraction; random forest; feature selection; fuzzy broad learning system; bearing fault diagnosis

Citation: Wu, L.; Zhang, C.; Qin, F.; Fei, H.; Liu, G.; Zhang, J.; Xu, S. Bearing Fault Diagnosis Method Based on Multi-Domain Feature Selection and the Fuzzy Broad Learning System. *Processes* **2024**, *12*, 369. https://doi.org/10.3390/pr12020369

Academic Editor: Olympia Roeva

Received: 13 December 2023
Revised: 21 December 2023
Accepted: 22 December 2023
Published: 10 February 2024

1. Introduction

Amidst the ongoing evolution of contemporary industrial and technological landscapes, an increasing number of intricately designed high-precision rotating machines are being conceptualized for the betterment of mankind. Bearings serve as crucial support tools in precision rotating machinery, facilitating relative positioning and load transfer between machine components [1]. Their pivotal role spans machine operation, maintenance, and overall reliability [2]. By survey statistics, approximately 30% of mechanical failures across diverse industrial domains can be attributed to issues associated with rolling bearings [3]. Hence, it has become an urgent and valuable task to study a method of fault feature extraction and pattern recognition with fast diagnostic speed and high diagnostic accuracy [4].

Since the vibration of machinery is directly linked to its structure, the vibration signal detected by sensors serves as a precise reflection of the bearing's operational state.

Consequently, vibration signal processing methods have emerged as a widely adopted technology for the diagnosis and detection of bearing faults. Currently, numerous scholars have garnered substantial outcomes, employing vibration signals to discern the operational nuances of rolling bearings. For instance, Zhang et al. [5] introduced an optimal periodic augmented group sparsity method, leveraging numerical properties of vibration signals and an ocean predator algorithm for the early extraction of bearing fault features. Zhao et al. [6] proposed an adaptive multi-band denoising model anchored in a Morlet wavelet filter and sparse representation, utilizing a Morlet wavelet filter, window envelope spectral kurtosis, and Hilbert transform to ascertain fault eigenfrequencies. Chen et al. [7] advanced two synchronized averaging frameworks rooted in instantaneous angular speed (IAS). The enhanced negative entropy index and the estimation properties of the synchronous averaging signal are harnessed to refine the characterization of rolling bearing faults. Tian et al. [8] advocated an adaptive variational modal decomposition (AVMDNS-FSC) method, incorporating noise suppression and fast spectral correlation. The AVMDNS algorithm dynamically selects parameters K and alpha to effectively suppress noise in the intrinsic mode function (IMF), thus facilitating the precise extraction of bearing fault features. Cheng et al. [9] devised a Sin-periodic modal decomposition (SPMD) method, introducing the singular value squared difference ratio (SVSDR) spectrum. The determination of the embedding size of the PSM is achieved through the Sin Geometric Similarity Transform, yielding the Sin Geometric Component Matrix (SGCM). The first Sin Geometric Periodic Component (SPC) is ascertained by Periodic Impact Intensity (PII), culminating in termination by the Spectral L2/L1 Paradigm (SNL2/L1) exponent for the accurate extraction of bearing fault characteristics. However, these methodologies typically necessitate manual extraction of signal fault characteristics, demanding engineers with extensive experience and expertise. Nevertheless, with the continuous expansion of data collected from industrial equipment, signal processing-based fault diagnosis methods are exhibiting limitations.

Deep learning methodologies have found extensive application in data-driven mechanical fault diagnosis, yielding noteworthy diagnostic outcomes. Furthermore, with the escalating volume of data, the diagnostic results of deep learning models also show better results. Sharma R et al. [10] introduced a framework integrating deep learning, meta-heuristics, and MCDM algorithms to identify thyroid-related abnormalities from ultrasound and histopathology images. Initially, three advanced deep learning techniques are employed to extract features from thyroid image datasets. Following this, six feature transformation techniques are studied to decrease data dimensionality, mitigating potential overfitting issues. Subsequently, five classifiers are assessed using a five-fold hierarchical cross-validation method. The first stage focuses on selecting the most effective feature extraction and classification techniques, while the second stage evaluates the optimal dimensionality reduction method using wrapper feature selection. This proposed approach outperforms current diagnostic methods, offering significant assistance to medical professionals in thyroid-related diagnostics. Wen et al. [11] introduced a novel Convolutional Neural Network (CNN) grounded in LeNet-5 architecture for fault diagnosis. This model automatically extracts diagnostic features by transforming one-dimensional signals into two-dimensional images, thereby achieving substantial advancements in diagnostic outcomes, surpassing both traditional and other deep learning methods. Li et al. [12] proposed a model for rolling bearing fault diagnosis, integrating a dual-level attention Recurrent Neural Network (DA-RNN) and a Convolutional Block Attention Module (CBAM). This model demonstrated considerable effectiveness in addressing fault diagnosis for imbalanced datasets. Gao et al. [13] presented an optimized Adaptive Deep Belief Network (SADBN), which significantly enhances the diagnostic accuracy of Deep Belief Networks (DBN). This improvement is achieved by pre-training the DBN through minimum batch stochastic gradient descent, followed by comprehensive supervision and fine-tuning of the entire DBN model. Various other deep learning methods for fault diagnosis, including Long Short-Term Memory Networks [14], Deep Residual Networks [15], and Stacked Autoencoders [16], along with their derivatives, have been explored. Despite the notable

strides made by deep learning methods in fault diagnosis, the training processes of most networks are inherently time consuming, attributed to the intricate structure of the network and the necessity for tuning a substantial number of hyperparameters. Moreover, if the fault diagnosis is not as accurate as expected, the deep learning network necessitates iterative parameter adjustments or the incorporation of additional network layers to enhance accuracy. These processes are notably time consuming and labor intensive [17].

In summary, inherent limitations exist in fault diagnosis when employing signal processing methods and deep learning techniques. In 2018, C. L. Philip Chen introduced a Flattened Broad Learning System (BLS) [18]. In contrast to the intricate network structure of deep learning, BLS comprises solely input and output layers, offering optimization through an increase in nodes in the augmentation layer, thereby mitigating network complexity. Unlike deep learning, which necessitates the calculation of weights between each neuron, BLS requires only the computation of connection weights from the input to output layers. This distinction effectively alleviates the drawback of prolonged training times [19]. Moreover, BLS allows for the extension of the network structure without necessitating complete network retraining [20]. Consequently, BLS addresses the challenges of extended training periods and the interpretability deficit inherent in deep learning, an increasing number of scholars are employing BLS in the realm of fault diagnosis. Fu et al. [21] proposed a Task-Incremental Broad Learning System (TiBLS) tailored for multi-component intelligent fault diagnosis. They introduced a structure-incremental learning capability for TiBLS to enhance individual tasks without retraining, yielding favorable results in experiments. Yang et al. [22] introduced a novel Twin BLS (TBLS) for the diagnosis of faults in rotating machinery. TBLS adeptly identifies two non-parallel hyperplanes to address classification issues, demonstrating heightened generalization capability in fault diagnosis scenarios for swift and effective diagnostic outcomes. Zhou et al. [23] proposed a variant of TBLS, integrating Principal Element Analysis and Singular Value Decomposition (IPS), designed for infrared fault diagnosis of rolling bearings. Additionally, they introduced a Stacked BLS (SSDStacked-BLS) model based on a self-selected depth model for expeditious fault diagnosis in bearings. Wang et al. [24] presented a TSK Fuzzy Broad Learning System (TSK-BLS), amalgamating the strengths of BLS and fuzzy systems. This model, utilizing pseudo-inverse and symmetric methods, stands as an efficient means for rapid and accurate fault diagnosis.

In the above studies of BLS, the traditional approach is to input raw fault data directly into the BLS for diagnosis. However, owing to the straightforward structure of the BLS, its feature extraction capability is deemed inadequate, consequently impacting diagnostic accuracy. Consequently, numerous scholars advocate the preprocessing of fault signals through multidomain extraction before inputting them into the BLS for bearing diagnosis. Wu et al. [25] introduced a multidomain feature fusion diagnostic approach for variable speed bearings, grounded in a generalized learning system. Lu et al. [26] devised an enhanced BLS fault diagnostic method incorporating data augmentation and multi-domain feature fusion. In this approach, time domain, frequency domain, and time-frequency domain features are extracted from vibration signals. The ReliefF algorithm is utilized for multi-domain feature selection, significantly improving diagnostic accuracy when input into the BLS. Zhang [27] proposed a robust BLS variant, BLS-QMEE, based on the quantized minimum error entropy (QMEE) criterion. Comparable to the standard BLS and other existing variants, BLS-QMEE demonstrates superior performance without substantial time consumption. Building on these advancements, this paper presents a bearing fault diagnosis method based on multi-domain feature selection and fuzzy BLS. Initially, the original fault signal undergoes multidomain feature extraction, encompassing time domain, frequency domain, time-frequency domain features, and entropy to construct the multidomain feature set. Subsequently, the importance of each original feature is calculated and ranked using the Random Forest method, facilitating the selection of the optimal feature subset. Finally, this feature subset is employed to train the FBLS, achieving efficient and precise intelligent fault diagnosis. To validate the efficacy of the proposed method, data collected from the

rolling bearing fault simulation test bed are utilized for validations. The results affirm the method's capability to realize efficient and highly accurate fault diagnosis.

The principal innovations of this paper encompass the following:

(1) A novel fault diagnosis method is introduced, integrating FBLS and multidomain feature selection. This innovative approach significantly enhances the accuracy of fault diagnosis within FBLS.

(2) A multi-domain feature extraction method is proposed, incorporating five types of entropy values, thereby expanding the original features in the multidomain feature set and establishing the groundwork for constructing features with heightened sensitivity to faults.

(3) A multi-domain feature selection method is proposed, utilizing the out-of-bag estimation function of Random Forest to identify features with heightened sensitivity to faults in the multidomain feature set as the optimal feature subset, consequently enhancing the diagnostic accuracy of the model.

2. Theoretical Background

2.1. Broad Learning System (BLS)

Addressing the prevalent challenges associated with the intricate structures and numerous hyperparameters of most deep learning networks, as well as their prolonged training processes, C. L. Philip Chen used the Broad Learning System (BLS) as an alternative, as outlined in his article published in January 2018. Initially applied in the domain of image recognition, the BLS distinguishes itself by its minimalist architecture comprising only two layers—namely the input layer A and the output layer Y—connected through weights W. This streamlined network structure incorporates feature enhancement nodes and output coefficient matrices, facilitating the rapid extraction of features from new data and minimizing retraining duration [28]. Consequently, the flat network of the BLS proves to be more efficient in addressing classification and regression challenges, obviating the necessity for a deep architecture. The architectural representation of the BLS is depicted in Figure 1.

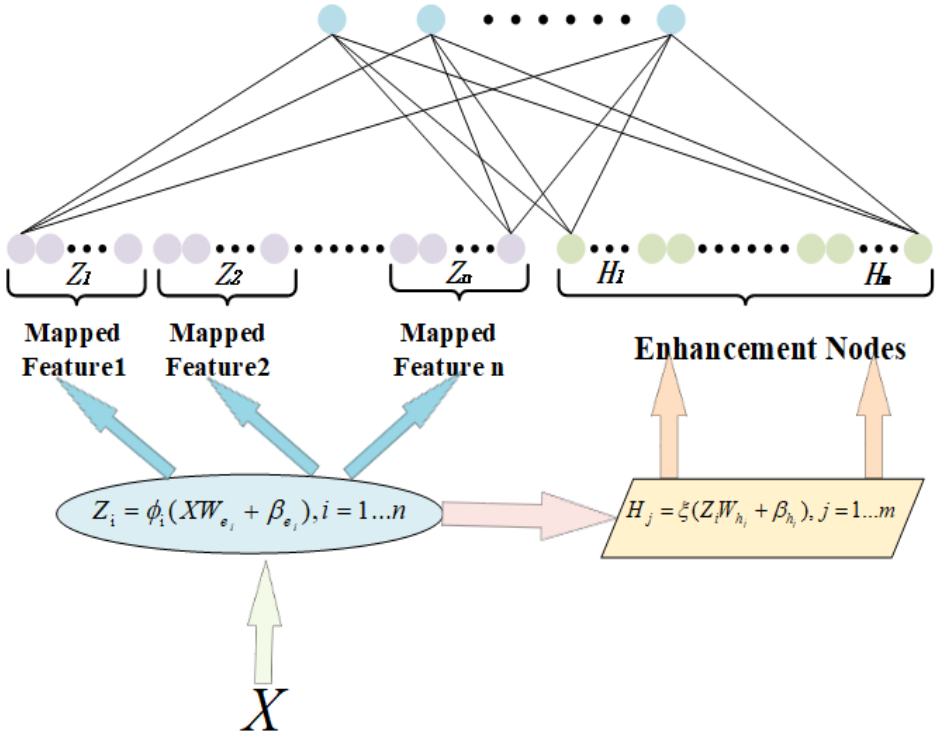

Figure 1. Broad learning system (BLS) architecture diagram.

2.2. Fuzzy Broad Learning System (FBLS)

Prof. C. L. Philip Chen's team combined the Takagi–Sugeno (TS) fuzzy system with the BLS to introduce a novel fuzzy neural network model termed Fuzzy Broad Learning (FBLS) [29]. FBLS maintains the core structure of BLS while integrating the TS fuzzy subsystem in lieu of BLS's feature nodes and eliminating the sparse self-encoder used for weight fine-tuning in the BLS feature layer, thereby simplifying the architecture [30]. This modification not only enables FBLS to retain the rapid computational properties of BLS, but also enhances the model's classification capability. Its overall architecture and the layout of the fuzzy subsystem are demonstrated in Figures 2 and 3.

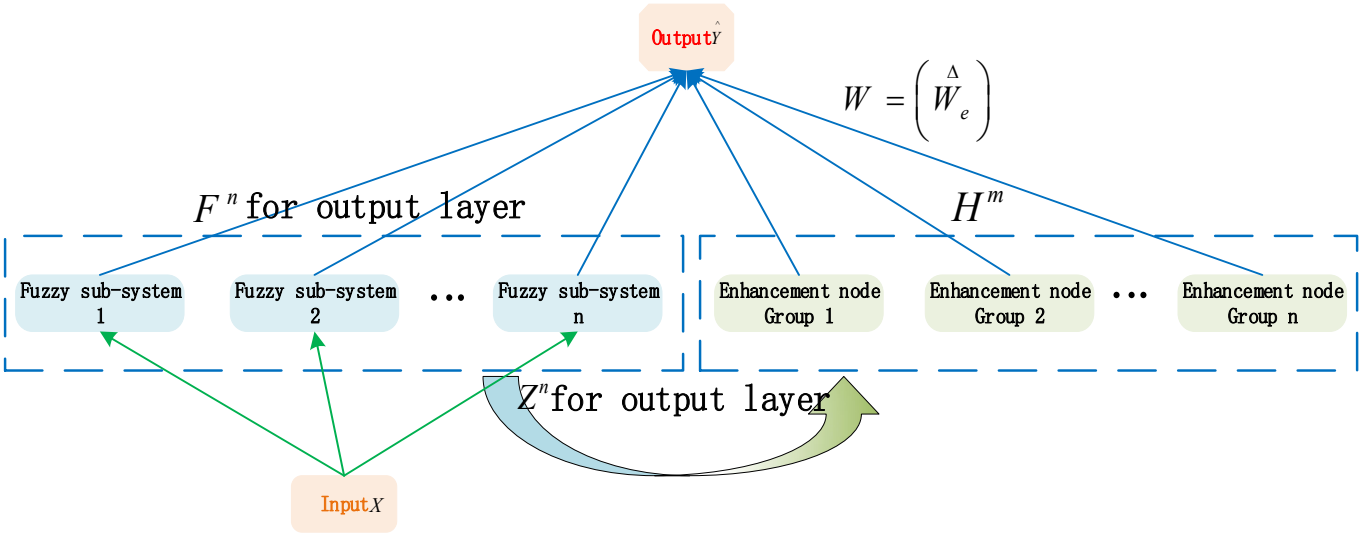

Figure 2. Structure of a fuzzy BLS.

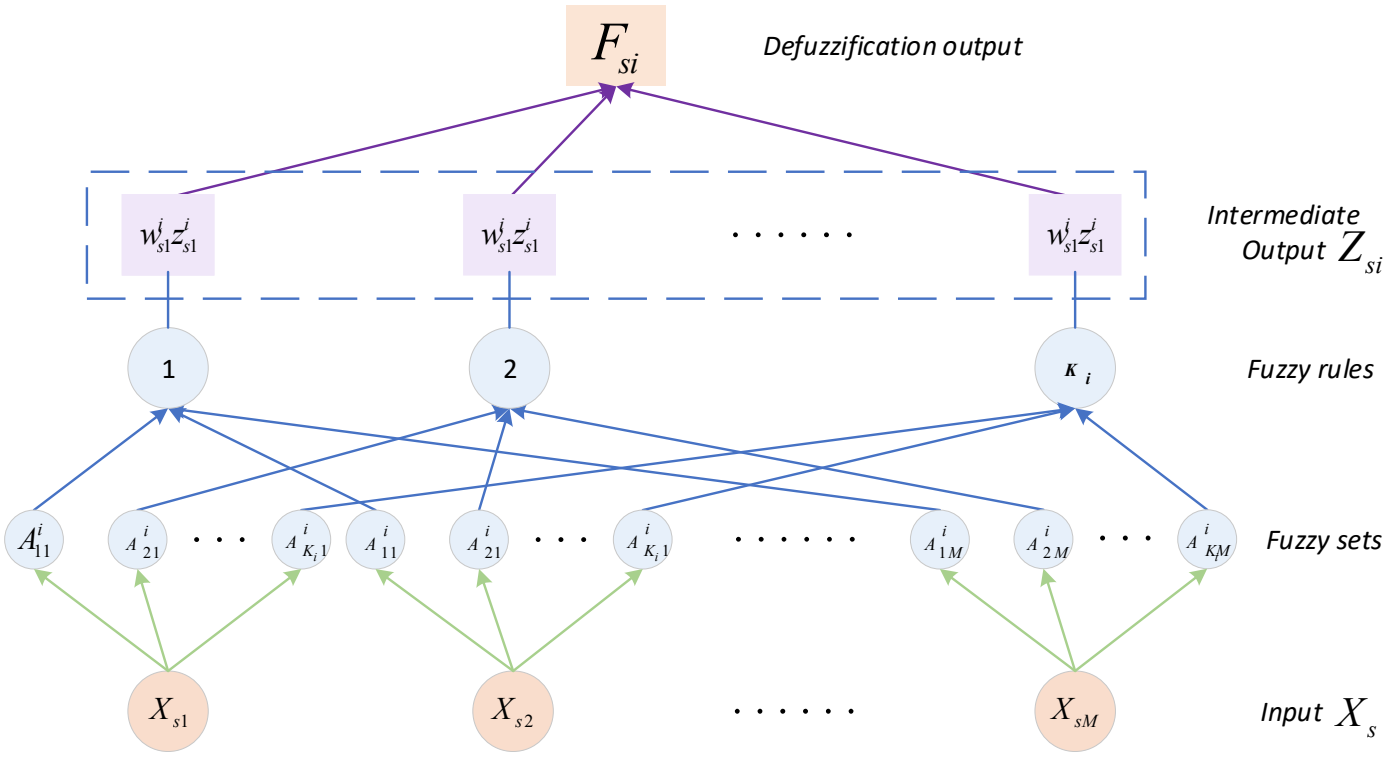

Figure 3. Structure of the *i*th fuzzy subsystem in a fuzzy BLS.

Within the FBLS framework, the inclusion of n fuzzy subsystems and m sets of augmented nodes is assumed. The input data follow this format: $X = (x_1, x_2, \ldots, x_{sN})^T \in R^{N \times M}$, where, $x_s = (x_{s1}, x_{s2}, \ldots, x_{sM}), s = 1, 2, \ldots, N$.

In the fuzzy subsystem structure, each subsystem is presumed to contain k fuzzy rules of the following format:

If x_{s1} is A^i_{K1}, x_{s2} is A^i_{K2} ..., x_{sM} is A^i_{KM}, then $z^i_{sk} = f^i_k(x_{s1}, x_{s2}, \ldots, x_{sM}),\ k = 1, 2, \ldots, k_i$.

The first-order fuzzy subsystem used in FBLS is

$$z^i_{sk} = f^i_k(x_{s1}, x_{s2}, \ldots, x_{sM}) = \sum_{t=1}^{M} \alpha^i_{kt} x_{st}, \tag{1}$$

where α^i_{kt} with its coefficients determined through pseudo-inverse calculation is initially set as random numbers from a uniform distribution in a range of [0, 1].

Within the fuzzy subsystem, the activation strength of the kth fuzzy rule in the ith fuzzy subsystem can be expressed as $\tau^i_{sk} = \prod_{t=1}^{M} \mu^i_{kt}(x_{st})$. Hence, the weight of each fuzzy rule can be expressed as follows: $\omega^i_{sk} = \frac{\tau^i_{sk}}{\sum_{k=1}^{K_i} \tau^i_{sk}}$. The chosen Gaussian affiliation function is defined as follows: $\mu^i_{kt}(x) = e^{-\left(\frac{x - c^i_{kt}}{\sigma^i_{kt}}\right)^2}$, where c^i_{kt} and σ^i_{kt} represent the width and the center, respectively.

To retain maximal information from the input data, FBLS defines a vector

$$Z_{si} = (\omega^i_{s1} Z^i_{s1}, \omega^i_{s2} Z^i_{s2}, \ldots, \omega^i_{sK_i} Z^i_{sK_i}), \tag{2}$$

where this vector comprises outputs from all fuzzy rules within the ith fuzzy subsystem, subsequently aggregated into a singular value representing the defuzzified output of the fuzzy subsystem. The resulting defuzzified output matrix is $Z_i = (Z_{1i}, Z_{2i}, \ldots, Z_{Ni})^T \in R^{N \times K_i}$, $i = 1, 2, \ldots, n$. Next, the intermediate vectors from all fuzzy subsystems are directed into the augmented node layer for further nonlinear transformations.

To maintain notation consistency, we represent the intermediate output matrix of the n fuzzy subsystems as $Z^n = (Z_1, Z_2, \ldots, Z_n) \in R^{N \times (K_1 + K_2 + \ldots + K_n)}$. Subsequently, it is forwarded to the augmentation nodes for nonlinear transformation. Assuming there are L_j neurons in the jth enhancement node group, we denote the output matrix of the enhancement layer as

$$H^m = (H_1, H_2, \ldots, H_m) \in R^{N \times (L_1 + L_2 + \ldots + L_m)}, \tag{3}$$

where $H_j = \xi_j(Z^n W_{hj} + \beta_{hj}) \in R^{N \times L_j}$ is the output matrix of the jth augmented node group, and W_{hj} and β_{hj} are the randomly generated weights and biases. Hence, the output of FBLS can be expressed as

$$\hat{Y} = F^n + H^m W_e, \tag{4}$$

where W_e is the weight between the enhancement layer and the output layer and $\hat{Y}$ is the output matrix.

2.3. Random Forests (RF)

Random Forests (RF) have emerged as a prevalent integration method in machine learning for addressing classification and regression problems [31]; its specific architecture is shown in Figure 4. Random Forests possess the ability to compute feature importance, thereby offering feature ranking [32]. While the average decrease in the Gini coefficient is a commonly employed metric for assessing feature importance, it has been acknowledged to possess certain limitations. In recent years, scholars have proposed a new feature ranking model: comparing mixed multi-criteria decision making (MCDM) to rank features [33]. Many scholars have also turned to the importance of substitution of variables, i.e., reflecting the importance of features by substituting the individual feature values of all samples. This

is achieved by calculating the average difference between accuracy rates on all trees before and after the substitution of eigenvalues for the Out of Bag (OOB) samples. The steps are as follows:

In the first stage, the OOB sample is placed on the jth tree and its accuracy is computed, denoted as $A_j^0, j = 1, 2, \ldots, ntree$.

In the second stage, for the ith feature, the values of OOB samples are replaced and the replaced samples are assessed on the jth tree to calculate its accuracy, denoted as $A_j^i, i = 1, 2, \ldots, n$ and $j = 1, 2, \ldots, ntree$.

In the third stage, the importance score for the ith feature, denoted as S_i, is obtained using the following equation:

$$S_i = \frac{1}{ntree} \sum_{j=1}^{ntree} (A_j^0 - A_j^i). \tag{5}$$

In the fourth stage, a descending list of feature importance score $\{S_{d_1}, S_{d_2}, \ldots, S_{d_n}\}$ is generated, where the vector represents the ranking of the features. A higher rank corresponds to greater feature importance.

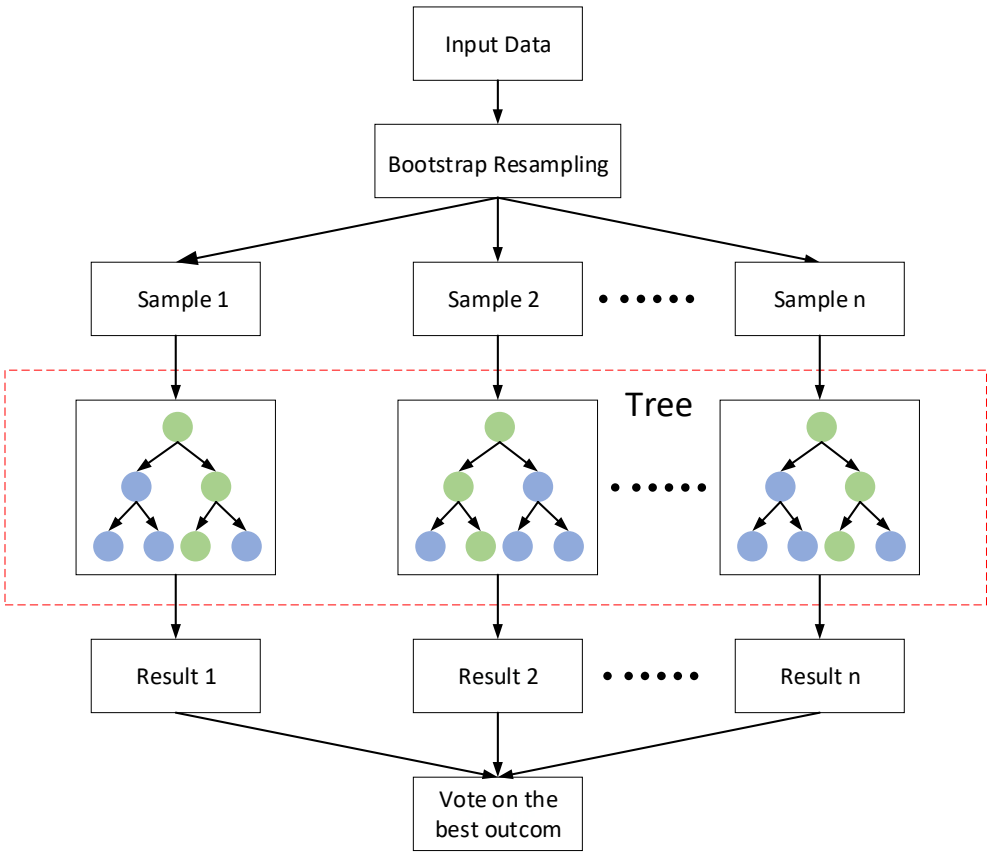

Figure 4. Random Forests (RF) architecture diagram.

2.4. Multidomain Feature Extraction

Through the application of statistical methodologies, 16 time-domain features and 13 frequency-domain features are derived from the original signals, and their nomenclature and mathematical expressions are delineated in the accompanying Tables 1 and 2. Notably, p_6 , p_{16} and p_{13} denote the kurtosis, peak, and pulse indicator, respectively; they are more sensitive to shock-type faults, especially when the fault occurs early, and they have a significant increase, but they are less stable. Concurrently, p_2 and p_7 represent the standard deviation and variance, respectively, serving as indices of data dispersion or

concentration. Additionally, p_8, p_9, and p_{10} correspond to the maximum value, minimum value, and peak-to-peak value, elucidating the amplitude fluctuation range within the signal. Furthermore, p_{17} signifies the magnitude of vibration energy within the frequency domain. Subsequently, parameters p_{26} to p_{29} signify the degree of dispersion or concentration within the frequency spectrum, while parameter up to p_{25} encapsulate variations in the positioning of the principal frequency band.

Table 1. Terminology and mathematical expressions for 16 time-domain features.

Feature Name	Formula	Feature Name	Formula
Average	$P_1 = \frac{1}{N}\sum_{n=1}^{N} x(n)$	Root mean square	$p_2 = \sqrt{\frac{1}{N}\sum_{n=1}^{N}[x(n)-p_1]^2}$
Root mean square amplitude	$p_3 = [\frac{1}{N}\sum_{n=1}^{N}\sqrt{\lvert x(n)\rvert}]^2$	Absolute averages	$p_4 = \frac{1}{N}\sum_{n=1}^{N}\lvert x(n)\rvert$
Skewness	$p_5 = \frac{1}{N}\sum_{n=1}^{N}[x(n)]^3$	Kurtosis	$p_6 = \frac{1}{N}\sum_{n=1}^{N}[x(n)]^4$
Variance	$p_7 = \frac{1}{N}\sum_{n=1}^{N}[x(n)-p_1]^2$	Maximum values	$p_8 = \max\lvert x(n)\rvert$
Minimum values	$p_9 = \min\lvert x(n)\rvert$	Peak-to-peak ratio	$p_{10} = p_8 - p_9$
Form factor	$p_{11} = \frac{p_2}{p_4}$	Peaking factor	$p_{12} = \frac{p_8}{p_3}$
Pulse factor	$p_{13} = \frac{p_8}{p_4}$	Clearance factor	$p14 = \frac{p_8}{p_3}$
Skewness coefficient	$p_{15} = \frac{p_5}{(\sqrt{p_7})^3}$	Kurtosis coefficient	$p_{16} = \frac{p_6}{(p_7)^2}$

Table 2. Terminology and mathematical expressions for 13 frequency-domain features.

Feature Name	Formula	Feature Name	Formula
Average frequency	$P_{17} = \frac{1}{K}\sum_{k=1}^{K} y(k)$	Frequency Standard deviation	$p_{18} = \frac{1}{K}\sum_{k=1}^{K}[y(k)-p_{17}]^2$
——	$p_{19} = \frac{\sum_{k=1}^{K}[y(k)-p_{17}]^3}{K(p_{18})}$	——	$p_{20} = \frac{\sum_{k=1}^{K}[y(k)-p_{17}]^4}{K(p_{18})}$
Center of gravity frequency	$p_{23} = \frac{\sum_{k=1}^{K}(f_k{}^2 y(k))}{\sum_{k=1}^{K} y(k)}$	Root mean square frequency	$p_{24} = \sqrt{\frac{\sum_{k=1}^{K}(f_k{}^4 y(k))}{\sum_{k=1}^{K}(f_k{}^2 y(k))}}$
——	$p_{25} = \frac{\sum_{k=1}^{K}(f_k{}^2 y(k))}{\sqrt{[\sum_{k=1}^{K}(f_k{}^4 y(k))][\sum_{k=1}^{K} y(k)]}}$	——	$p_{26} = \frac{p_{22}}{p_{21}}$
——	$p_{27} = \frac{\sum_{k=1}^{K}[(f_k-p_{21})^3 y(k)]}{K(p_{22})^3}$	——	$p_{28} = \frac{\sum_{k=1}^{K}[(f_k-p_{21})^4 y(k)]}{K(p_{22})^4}$
——	$p_{29} = \frac{\sum_{k=1}^{K}[\sqrt{\lvert f_k-p_{21}\rvert} y(k)]}{K\sqrt{p_{22}}}$	——	——

Given that the original vibration signals typically exhibit nonlinearity and nonsmoothed characteristics, and recognizing the heightened efficacy of time-frequency domain analysis methods in extracting fault features from nonsmoothed signals [14], the wavelet packet transform (WPT) is applied to the original vibration signals for the extraction of wavelet energy indicators across distinct frequency bands. The specific computational steps for extracting the time-frequency domain features are as follows:

In the first stage, the WPT is employed to decompose $x(n)$ into multiple sub-signals. Subsequently, the wavelet packet coefficients are defined as [33]

$$S_{l_j} = [S^1{}_{l_j}, S^2{}_{l_j}, \ldots, S^{\frac{n}{2^l}}{}_{l_j}], \tag{6}$$

where l signifies the number of layers in the wavelet packet and j denotes the number of sub-signals.

In the second stage, wavelet energy metrics are calculated for each frequency band, which is defined by equation

$$E_{l_j} = \sum_{K=1}^{\frac{n}{2^l}} \left| S^k{}_{l_j} \right|. \tag{7}$$

In the third stage, E_{l_j} is normalized as defined below:

$$\widehat{E_{l_j}} = \frac{E_{l_j}}{\sum\limits_{m=1}^{2^l} E_{lm}}. \tag{8}$$

In this study, l is set to three, and j is eight. The wavelet energy values are arranged in a descending order, and the first four wavelet energy indicators are selected as the time-frequency domain features $p_{30} \sim p_{33}$, which encapsulate a substantial volume of fault-related information.

To capture the maximum information embedded within the original vibration signal, Variational Mode Decomposition (VMD) is applied to the original vibration signal for calculating the energy entropy, fuzzy entropy, alignment entropy, and sample entropy of each Intrinsic Mode Function (IMF). Taking the entropy on energy as an example, the specific steps are as follows:

In the first stage, VMD decomposition of the original vibration signal $x(n)$ is performed to obtain m IMF:

$$VMD[x(n)] = \sum_{i=1}^{m} IMF_i(t) + r_m. \tag{9}$$

In the second stage, the energy of each Intrinsic Mode Function (IMF) is computed using the following expression:

$$Ei = \int_{-\infty}^{+\infty} |IMF_i(t)|^2 \, dt, \tag{10}$$

where $IMF_i(t)$ represents the ith obtained post VMD, with $i = 1, 2, \ldots, m$.

In the third stage, given the orthogonality of VMD, implying that the sum of energies across all IMF components equals the total energy of the original vibration signal,

$$E = \sum_{i=1}^{m} E_i, \tag{11}$$

$$P_i = \frac{E_i}{E}, \tag{12}$$

where P_i is the ratio of the energy $IMF_i(t)$ to the total energy of the original signal E.

In the third stage, the entropy of energy is calculated using the following expression:

$$H_{EN} = -\sum_{i=1}^{m} P_i \log P_i. \tag{13}$$

The primary fault information tends to reside within the initial IMF components of the original signal [15], this study selectively employs the first four sub-signals for computing various entropy measures. Specifically, it calculates energy entropy: $p_{34} \sim p_{37}$, fuzzy entropy $p_{38} \sim p_{41}$, arrangement entropy $p_{42} \sim p_{45}$, sample entropy $p_{46} \sim p_{49}$. These 16 entropy values collectively encompass a substantial amount of fault-related information.

Ultimately, the multi-domain feature dataset from each data sample is amalgamated to formulate the High-Vitae Feature Set (HFD)

$$HFD = \begin{bmatrix} p_1 & p_8 & p_{15} & p_{22} & p_{29} & p_{36} & p_{43} \\ p_2 & p_9 & p_{16} & p_{23} & p_{30} & p_{37} & p_{44} \\ p_3 & p_{10} & p_{17} & p_{24} & p_{31} & p_{38} & p_{45} \\ p_4 & p_{11} & p_{18} & p_{25} & p_{32} & p_{39} & p_{46} \\ p_5 & p_{12} & p_{19} & p_{26} & p_{33} & p_{40} & p_{47} \\ p_6 & p_{13} & p_{20} & p_{27} & p_{34} & p_{41} & p_{48} \\ p_7 & p_{14} & p_{21} & p_{28} & p_{35} & p_{42} & p_{49}. \end{bmatrix} \tag{14}$$

3. Proposed Program

Rolling bearings, being susceptible components in machinery, pose a significant risk of economic losses and, in severe instances, casualties upon failure. Therefore, it is an urgent task to study a fault diagnosis method with fast diagnostic speed and high diagnostic accuracy. This section introduces the MS-FBLS model, showcasing its general framework illustrated in Figure 5. In order to filter the raw data for features that are more sensitive to faults, a multidomain feature pool is constructed by selecting 49 features from the time domain, frequency domain, time-frequency domain, and entropy value, and the optimal subset of features is selected from the multidomain feature pool using the Random Forest method, and it is inputted into the FBLS prediction model to improve the accuracy of the model. It is specifically divided into three steps:

(1) Acquisition of Vibration Signals: Vibration signals of distinct fault types are acquired, originating from the same rotational speed, employing accelerometers.

(2) Feature Extraction and Selection Across Multiple Domains for Vibration Signals: A comprehensive multi-domain feature extraction is executed for each sample, encompassing 49-dimensional features from the time domain, frequency domain, time-frequency domain, and entropy values to construct a comprehensive multi-domain feature set, therefore enhancing FBLS capability in feature extraction. In this investigation, Random Forest feature selection was employed to eliminate redundant information. Through the assessment of feature importance, the high-dimensional feature set underwent reorganization based on the individual significance levels of each feature.

(3) FBLS-Based Fault Classification: The 49-dimensional features are systematically inputted into the FBLS model, adhering to feature weights in descending order, thereby effectuating the fault classification of rolling bearings.

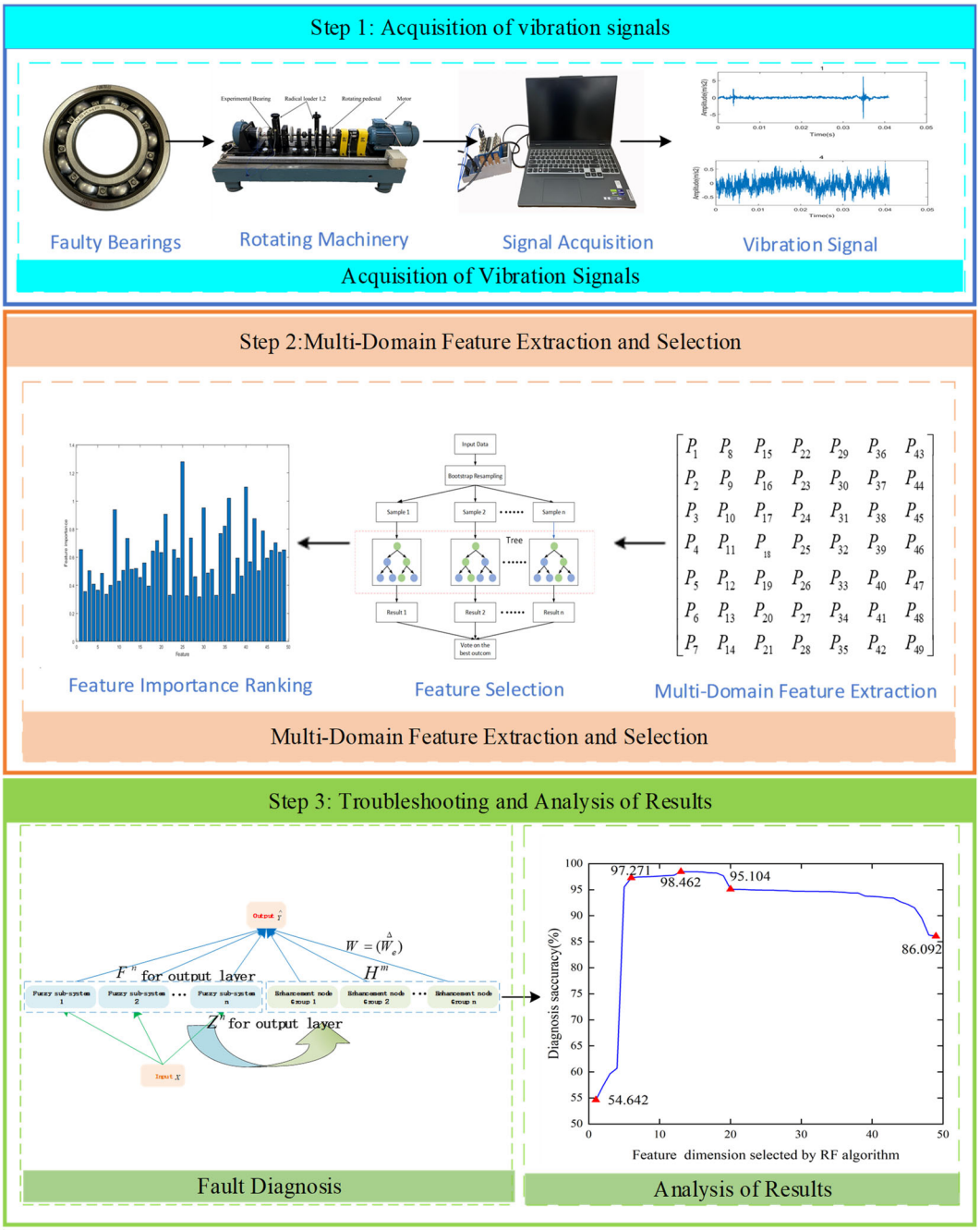

Figure 5. General architecture of the MS-FBLS.

4. Experiment and Analysis

To substantiate the efficacy of our proposed method, we meticulously devised a rolling bearing fault simulation test bed. This allowed for a comparative analysis between the MS-FBLS, the original vibration signal + FBLS, and multi-domain feature extraction + FBLS, demonstrating the superiority of our approach.

4.1. Experimental System Description and Data Collection

To validate the efficacy of the proposed methodology, we conducted a simulated experiment on artificial bearing failure utilizing the HZXT-DS-003 double-span double-rotor rolling bearing test stand, depicted in Figure 6. The experimental setup comprised a bearing housing, a radial loader, a speed torque meter, and a motor. HZXT-DS-003 featured a basic table size of 2000 × 800 mm. The drive system consisted of a 7.5 KW inverter motor operating at 380 V

with a speed range of 0–3000 R/min. Additionally, a vectorized three-phase inverter rated at 380 V 10 KW was utilized. The experimental apparatus comprised a bearing housing, a radial loader, a speed torque meter, and a motor. The rolling bearing model employed is denoted as radial ball bearings—6205-2RS, detailed data, as shown in Table 3, featuring nine distinct categories of bearing faults, as depicted in the accompanying Figure 7. Among these, three variations of inner ring faults, each characterized by different fault sizes (0.2 mm, 0.6 mm, 1.2 mm), are designated as OR1, OR2, and OR3, respectively. Similarly, three types of outer ring faults, with varying fault sizes (0.2 mm, 0.6 mm, 1.2 mm), are identified as IR1, IR2, and IR3. Furthermore, three categories of pitting faults—manifesting in the inner ring, outer ring, and rolling element—are recorded as OR4, IR4, and B1, respectively. Specific fault dimensions and labels are shown in Table 4. Accelerometers were employed to capture bearing data from the housing, resulting in the acquisition of nine distinct faulty vibration signals and one normal vibration signal. The nomenclature and labels for these faults are elucidated in Table 3. Throughout the experimental regimen, the rotational speed of the shafts was maintained at 1500 r/min, with all vibration signals recorded at a consistent sampling frequency of 1.2 KHz.

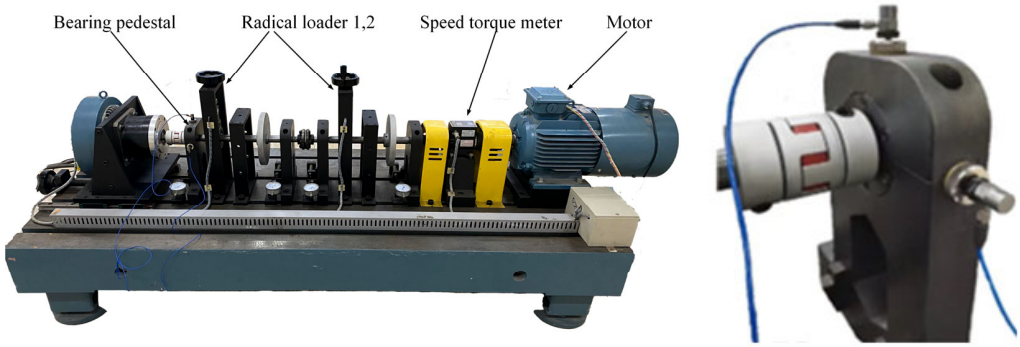

(**a**) (**b**)

Figure 6. (**a**) HZXT-DS-003 double-span double-rotor rolling bearing test bench; (**b**) Location of vibration sensors.

Table 3. Detailed data of radial ball bearings—6205-2RS.

Bearing Type	Inside Diameter Sized	Outer Diameter Size	Roller Diameter	Number of Rollers
6205	25 mm	52 mm	7.938 mm	9

Table 4. Dimensions and labels for 10 fault types.

Fault Type	Fault Size/mm	Label
Inner ring failure	0.2	IB1
	0.6	IB2
	1.2	IB3
	0.17	IB4
Outer ring fault	0.2	OB1
	0.6	OB2
	1.2	OB3
	0.17	OB4
Rolling element fault	0.17	B1
Normal	0	N

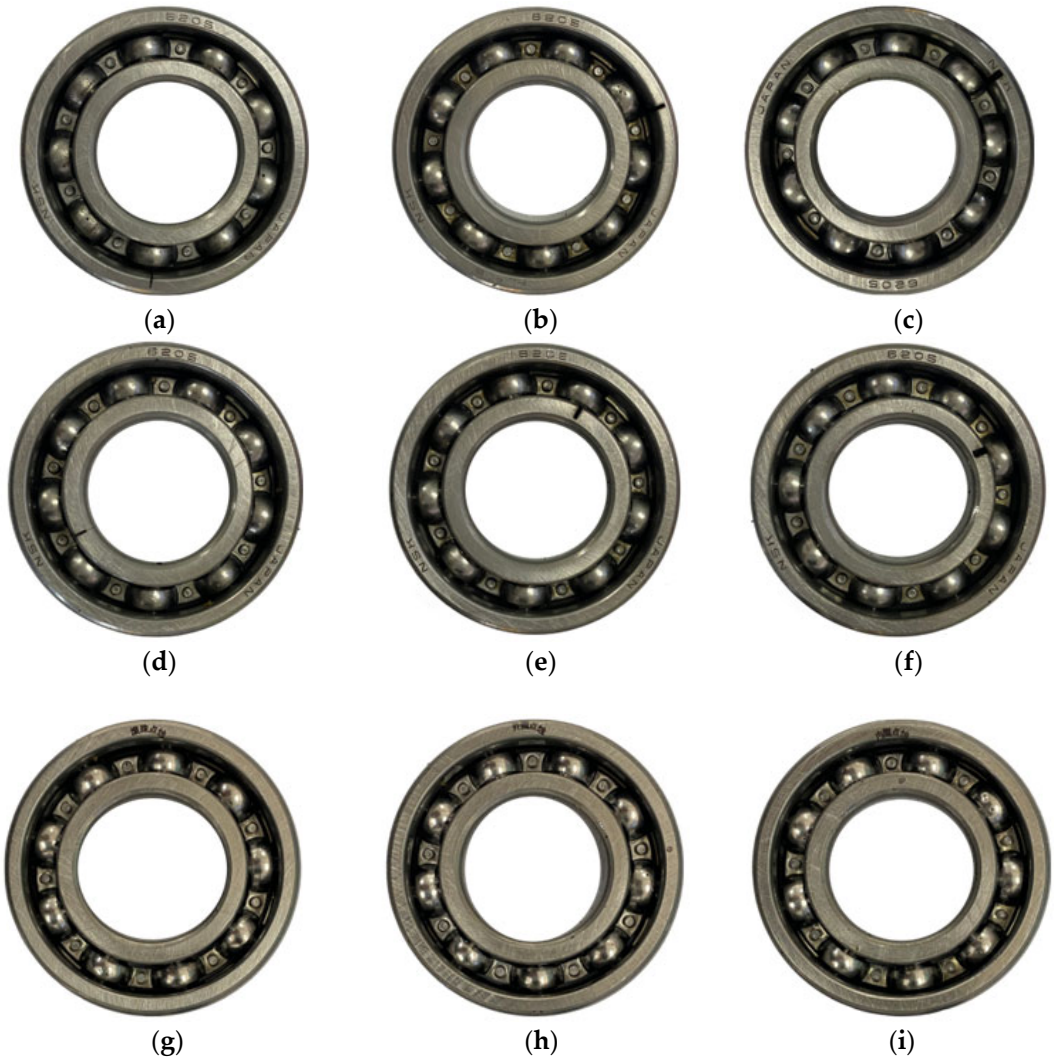

Figure 7. (**a**) Outer ring, 0.2 mm; (**b**) Outer ring, 0.6 mm; (**c**) Outer ring, 1.2 mm; (**d**) Inner ring, 0.2 mm;(**e**) Inner ring, 0.6 mm; (**f**) Inner ring, 1.2 mm; (**g**) Pitting of rolling element, 0.17 mm; (**h**) Pitting of outer ring, 0.17 mm; (**i**) Pitting of inner ring, 0.17 mm.

To capture sufficient fault information within each sample from the original vibration signal, the sample length surpasses the number of sampling points in one cycle of bearing rotation. The sampling frequency is 12 KHz, meaning that the acquisition card captures 12,000 vibration signals from the bearing per second. With the bearing rotating at a speed of 1500 r/min (equivalent to 25 revolutions per second), the calculated number of sampling points within one cycle of rotation is 480. To incorporate a more extensive range of fault-related data, the sample length is chosen to encompass the number of sampling points derived from two cycles, totaling 1024. Each fault type consists of 400 samples, summing up to 4000 samples in total. From each fault sample, 70 samples are randomly selected for training, while 30 samples are designated for testing, resulting in 2800 training samples and 1200 test samples. The FBLS model configuration encompasses 100 feature nodes and 100 enhancement nodes. Given the randomly generated weights within the FBLS, 50 experiments are conducted for each fault sample to generate outcomes from these 50 experiments.

4.2. Results of Feature Extraction and Feature Selection

To confirm the substantial enhancement in accuracy facilitated by the MS-FBLS model, three comparative experiments were conducted within the study:

(1) Inputting ten types of raw vibration signals directly into FBLS for fault diagnosis.

(2) Application of multidomain feature extraction to the original vibration signals to formulate high-dimensional feature sets, subsequently input into the FBLS for fault diagnosis.

(3) Performing multi-domain feature extraction on the original vibration signal, followed by RF calculation of feature importance within the multi-domain feature set, then inputting these features from highest to lowest importance into FBLS for fault diagnosis.

The experimental results are shown in Table 5 and Figure 8.

Table 5. Results of three comparative experiments.

Model	Training Accuracy	Testing Accuracy	Training Time
Raw vibration signal + FBLS	80.8%	75%	0.21 s
Multidomain feature extraction + FBLS	97.3%	86.9%	0.15 s
Multi-domain feature extraction + RF + FBLS	100%	98.46%	0.11 s

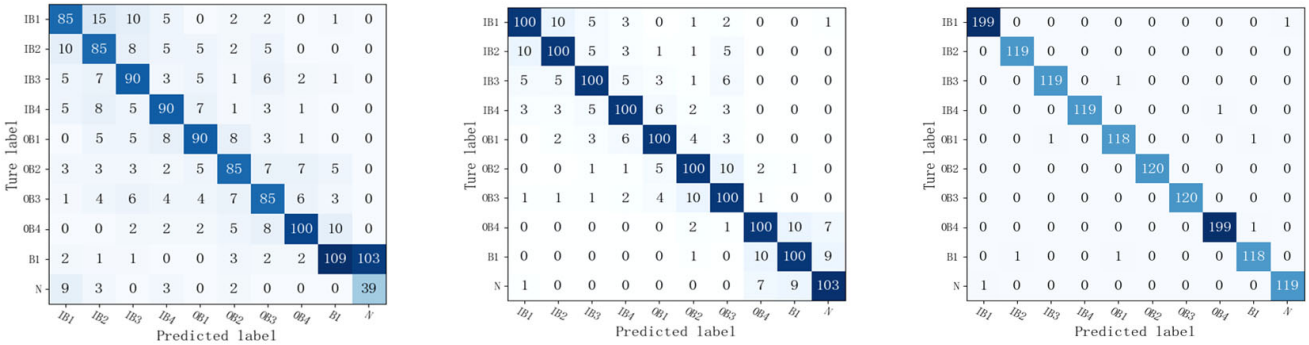

(**a**) (**b**) (**c**)

Figure 8. (**a**) Raw vibration signal + FBLS; (**b**) Multidomain feature extraction + FBLS; (**c**) Multi-domain feature extraction + RF + FBLS.

In the first model, the test accuracy registers at 75%, and the training time stands at 0.21 s. While the diagnostic speed of FBLS demonstrates a significant improvement compared to that of deep learning, the accuracy of the model directly inputting raw vibration signals into FBLS is not optimal. Hence, the implementation of multi-domain feature extraction on the raw vibration signals, leading to the construction of a high-dimensional feature set, emerges as one of the effective methodologies for enhancing the diagnostic accuracy of FBLS.

In the second model, a set of 49-dimensional multidomain features is extracted for each sample, and the resulting high-dimensional feature set is directly input into the FBLS for fault diagnosis. The average of 50 experimental results indicates an impressive test accuracy of 86.09%, and the training time is 0.15 s. In comparison to the first model, this demonstrates a substantial enhancement in diagnostic accuracy coupled with a significant reduction in training time, validating the efficacy of the multi-domain feature extraction method. Nevertheless, the application of feature selection to the multi-domain feature set using Random Forest (RF) becomes imperative due to the extended training time and diminished test accuracy arising from redundant information within the high-dimensional feature set.

In the third comparative model, the significance of each feature within the multidomain feature set is evaluated through Random Forest (RF), resulting in feature ranking; the importance of features is shown in Figure 9. The horizontal coordinates, ranging from 1 to 49, correspond to the features p1 through p49, while the vertical coordinates denote the respective feature importance. Following this, the multidomain feature set is rearranged based on feature importance, organizing them from highest to lowest in the following sequence:

$p_{25} > p_{40} > p_{36} > p_{30} > p_9 > p_{21} > p_{42} > p_{35} > p_{44} > p_{34} > p_{27} > p_{12} > p_{19} > p_{47} > p_{23} > p_1 > p_{49} > p_{46} > p_{18} > p_{48} > p_{20} > p_{45} > p_{38} > p_{24} > p_{41} > p_{16} > p_{14} > p_{13} > p_{32} > p_{11} > p_{43} > p_3 > p_{31} > p_6 > p_{39} > p_{28} > p_{15} > p_{10} > p_4 > p_8 > p_{17} > p_5 > p_2 > p_7 > p_{37} > p_{22} > p_{33} > p_{26} > p_{29}$

Observing the results, it becomes evident that feature p25 holds the highest importance, while feature p29 exhibits the lowest importance within RF algorithm analysis. In RF algorithms, features with higher importance are more advantageous for model training and thus should be preserved. Conversely, the lower the feature importance, the more useless or redundant the feature, and it needs to be eliminated.

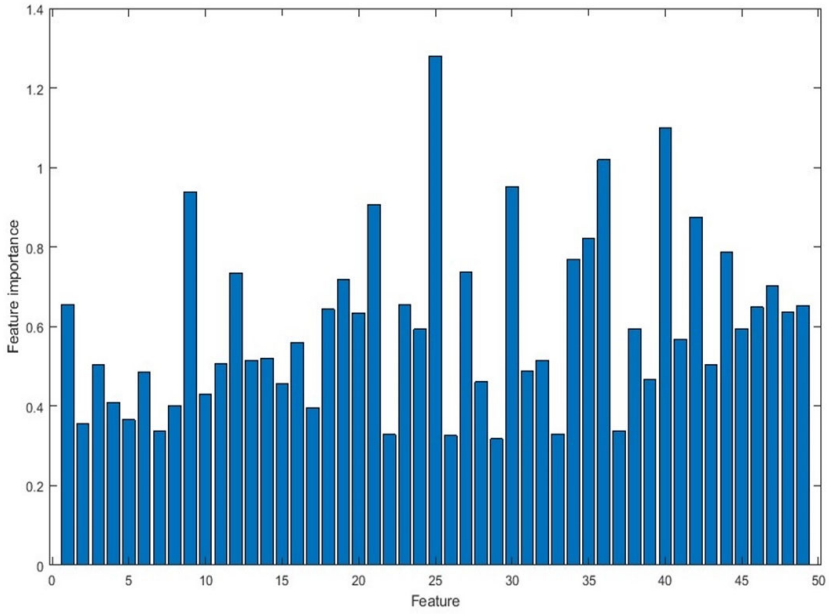

Figure 9. Importance ranking of features.

Currently, there is no established systematic method for determining the optimal subset of features to input into the FBLS. To select the best subset of features that are sensitive to faults, redundant features are eliminated. Hence, the features, sorted by descending importance, are sequentially fed into the FBLS following their respective order of significance, arranged from highest to lowest importance. The evolution in diagnostic accuracy is depicted in Figure 10. Notably, at a feature dimension of 1, the accuracy stands at 54.642%. This suggests a limitation due to the fewer useful features available, resulting in decreased accuracy in fault classification due to reduced information inclusion. When expanding the feature dimension to 13, the test accuracy peaks at 98.462%, marking the point of maximum diagnostic precision. However, as feature dimensions gradually increase, they incorporate redundant information, leading to a subsequent decline in accuracy. Eventually, as the feature dimension hits 49, the fault diagnosis accuracy settles at 86.09%.

To further validate the effectiveness of the RF algorithm for feature selection, a comparative analysis is conducted with two widely employed feature selection algorithms: ReliefF (RL) and Laplacian Score (LS). In the RL algorithm, varying weights are assigned to features based on their relevance to the respective categories. Features with weights falling below a certain threshold are subsequently removed. The LS algorithm assesses the local retention capability of features to gauge their importance. Figure 11 illustrates the accuracy of the three feature selection methods across different feature dimensions. According to the results, when the feature dimension is below 15, the RF algorithm exhibits significantly higher accuracy compared to RL and LS. Notably, LS attains the highest accuracy (96.36%) with a feature dimension of 13, RL achieves peak accuracy (97.67%) with a feature dimension of 17, while the RF algorithm attains its highest diagnostic accuracy (98.46%) at a feature dimension of 13. The RF feature selection algorithm outperforms the other algorithms in terms of test accuracy. Additionally, at the point of achieving the highest test accuracy, RF and LS share identical feature dimensions. The relationship between feature dimensionality and classification time is widely acknowledged—an increase in feature dimension prolongs

the classification process. Taking into consideration both feature accuracy and diagnosis time, RF feature selection proves to be the most efficient approach.

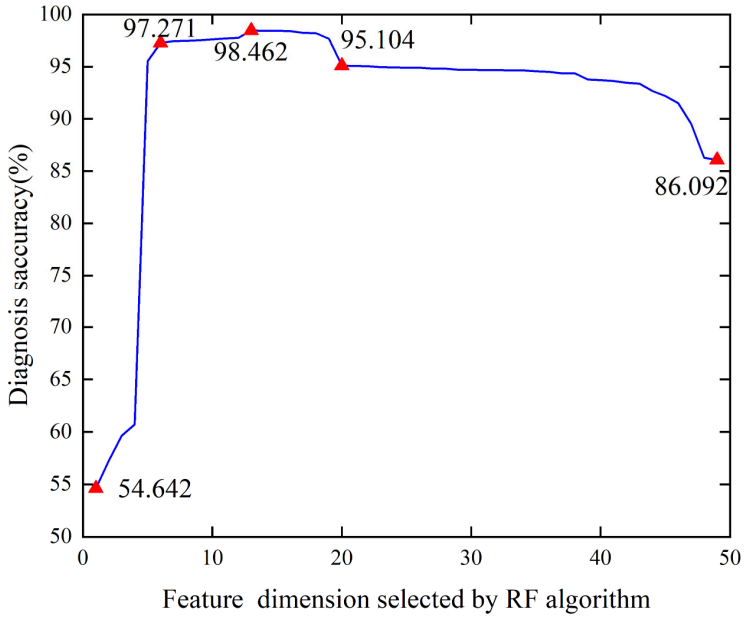

Figure 10. The evolution of diagnostic accuracy.

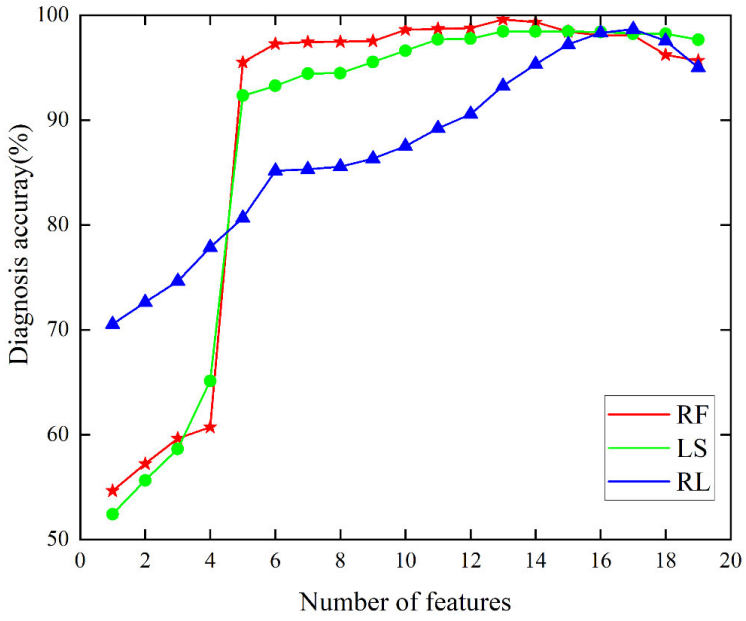

Figure 11. The accuracy of the three feature selection methods.

To further assess the effectiveness and superiority of the MS-FBLS model, a comparative experiment is conducted with different methods. Leveraging the multi-domain feature extraction algorithm outlined in Section 2.3, 49 multi-domain features, alongside 16 time-domain features, 13 frequency-domain features, 4 time-frequency-domain features, and 16 entropy-value features, are extracted, forming five distinct feature sets. These sets are then individually input into four classifiers for fault classification. The diagnostic results, as depicted in Table 6, highlight that the accuracy of multi-domain features surpasses that of features extracted from other domains. Specifically, the average accuracy achieved by combining multi-domain features with different classifiers is 98.06%. This substantiates the richer feature information offered by multi-domain features, contributing significantly

to the overall improvement in classification accuracy. Indeed, the comparison of accuracy reaffirms the superiority of multi-domain feature extraction.

Table 6. Diagnostic results graphs for the 5 models.

	Multidomain	Time Domain	Frequency Domain	Time-Frequency Domain	Entropy
FBLS	98.46%	89.33%	93.55%	89.73%	92.76%
SVM	97.00%	86.67%	93.36%	86.89%	87.23%
RNN	97.53%	88.52%	96.74%	95.25%	94.51%
ELM	98.25%	88.69%	97.55%	93.26%	89.43%
Average accuracy (%)	98.06%	88.30%	95.30%	91.28%	90.98%

5. Discussion

Rolling bearings, among the most vulnerable components in machinery, can incur substantial economic losses and, in severe cases, result in casualties if they fail. Therefore, the fault diagnosis of bearings needs to study both diagnostic accuracy and diagnostic speed. In this paper, the MS-FBLS model is proposed to address the limitations of existing fault diagnosis methods.

To validate the efficacy of the MS-FBLS model, a comparison was made between the model and the original vibration signal + FBLS model. It was observed that while FBLS offers rapid diagnosis, its accuracy remains relatively low. Therefore, the construction of a multidomain feature set emerges as an effective approach to enhance FBLS. Similarly, comparing MS-FBLS with a multidomain feature extraction + FBLS model, it was noted that the multidomain feature set contains excessive redundant information, affecting diagnostic accuracy. Hence, employing RF for feature importance calculation proves to be an effective means to eliminate such redundancy. Subsequently, all features in the multidomain set are input into the FBLS model based on their importance, leading to fault diagnosis characterized by both high accuracy and swift diagnosis. To further substantiate the effectiveness of the RF algorithm in feature selection, this study conducts a comparative analysis between RF and other algorithms such as RL and LS. The results distinctly favor the RF algorithm as the most effective. Additionally, the study investigates the efficacy of multidomain features by extracting 49 multidomain features, including 16 time-domain features, 13 frequency-domain features, 4 time-frequency-domain features, and 16 entropy-value features from vibration signals to form five distinct feature sets. These sets are input into four classifiers for fault classification. The findings reveal that multidomain features encompass richer information compared to single-domain features, consequently enhancing classification accuracy.

While the paper experimentally validates the efficacy of the proposed method, it also underscores certain limitations. The MS-FBLS model's effectiveness, demonstrated through experiments on the HZXT-DS-003 test bed, relies on a dataset primarily focused on common simulated faults in rolling bearings. This dataset is clear, singular, sufficiently standardized, and optimized for better experimental results. However, real-world operational conditions entail complexities and significant noise interference. Our forthcoming focus aims to adapt this model to real production environments.

6. Conclusions

To enhance the operational efficiency and dependability of machinery and equipment, the paper introduces an MS-FBLS fault diagnosis method that addresses the low-accuracy issue in FBLS fault diagnosis through multi-domain feature extraction and selection, and tackles the low diagnostic efficiency problem of depth learning by employing FBLS. The validation of the proposed MS-FBLS model is conducted using a rolling bearing fault simulation test bed, yielding the following conclusions from the experiments:

(1) High Efficiency of FBLS: Compared to deep learning methods, FBLS exhibits significantly shorter training times, showcasing its high efficiency.

(2) Advantages of Multi-Domain Features: In contrast to traditional single feature-based fault classification methods, multidomain features comprehensively reflect fault information, leading to superior recognition results.

(3) Random Forest's Superiority in Feature Selection: The Random Forest algorithm excels in feature selection, effectively removing redundant or irrelevant features in bearing fault classification and enhancing fault diagnosis computational capabilities.

In summary, the proposed MS-FBLS method shows substantial promise in bearing fault diagnosis, especially in enhancing diagnostic accuracy and reducing computational costs. Randomly generating weights in FBLS poses a challenge as the model lacks autonomous capacity to determine the optimal structure. There's potential for improvement in optimizing the structure search for achieving better results. Our forthcoming efforts will be dedicated to enhancing this aspect.

Author Contributions: Writing—original draft preparation, L.W.; project administration, C.Z.; resources, F.Q.; data curation, H.F.; modifications, G.L., J.Z. and S.X. All authors have read and agreed to the published version of the manuscript.

Funding: The support for this research from the National Natural Science Foundation of China (No: 51965052 and 52365014), the Central Government's Guidance in Local Science and Technology Development (No: 2022ZY0221) and Inner Mongolia Key Laboratory of Intelligent Diagnosis and Control of Mechatronic System is gratefully acknowledged.

Data Availability Statement: The rolling bearing dataset was obtained from the HZXT-DS-003 Double Span Double Rotor Rolling Bearing Test Stand at the School of Mechanical Engineering, Inner Mongolia University of Science and Technology.

Conflicts of Interest: The authors declare no conflicts of interest.

References

1. Patil, A.; Desai, S.; Patil, L.; Patil, S. Adopting artificial neural network for wear investigation of ball bearing materials under pure sliding condition. *Appl. Eng. Lett. J. Eng. Appl. Sci* **2022**, *7*, 81–88. [CrossRef]
2. Desnica, E.; Asonja, A.; Radovanovic, L.; Palinkas, I.; Kiss, I. Selection, Dimensioning and Maintenance of Roller Bearings. In Proceedings of the 31st International Conference on Organization and Technology of Maintenance (OTO), Josip Juraj Strossmayer Univ. Osijek, Fac Elect Engn, Comp Sci & Informat T, Osijek, Croatia, 12 December 2022; pp. 133–142.
3. Zhu, Z.Q.; Lei, Y.B.; Qi, G.Q.; Chai, Y.; Mazur, N.; An, Y.Y.; Huang, X.H. A review of the application of deep learning in intelligent fault diagnosis of rotating machinery. *Measurement* **2023**, *206*, 112346. [CrossRef]
4. Yang, B.; Lei, Y.G.; Jia, F.; Li, N.P.; Du, Z.J. A Polynomial Kernel Induced Distance Metric to Improve Deep Transfer Learning for Fault Diagnosis of Machines. *IEEE Trans. Ind. Electron.* **2020**, *67*, 9747–9757. [CrossRef]
5. Zhang, S.C.; Jiang, H.K.; Yao, R.H.; Zhu, H.X. Optimal periodicity-enhanced group sparse for bearing incipient fault feature extraction. *Meas. Sci. Technol.* **2023**, *34*, 085101. [CrossRef]
6. Zhao, L.J.; Zhang, L.; Zhang, H.; Hu, Y.Q. Bearing fault-induced feature enhancement via adaptive multi-band denoising model. *Meas. Sci. Technol.* **2023**, *34*, 075012. [CrossRef]
7. Chen, X.; Guo, Y.; Na, J. Instantaneous-Angular-Speed-Based Synchronous Averaging Tool for Bearing Outer Race Fault Diagnosis. *IEEE Trans. Ind. Electron.* **2023**, *70*, 6250–6260. [CrossRef]
8. Tian, S.N.; Zhen, D.; Liang, X.X.; Feng, G.J.; Cui, L.L.; Gu, F.S. Early fault feature extraction for rolling bearings using adaptive variational mode decomposition with noise suppression and fast spectral correlation. *Meas. Sci. Technol.* **2023**, *34*, 065112. [CrossRef]
9. Cheng, J.; Yang, Y.; Shao, H.D.; Cheng, J.S. Symplectic period mode decomposition method and its application in fault diagnosis of rolling bearing. *J. Vib. Control* **2023**. [CrossRef]
10. Sharma, R.; Mahanti, G.K.; Panda, G.; Rath, A.; Dash, S.; Mallik, S.; Hu, R. A Framework for Detecting Thyroid Cancer from Ultrasound and Histopathological Images Using Deep Learning, Meta-Heuristics, and MCDM Algorithms. *J. Imaging* **2023**, *9*, 173. [CrossRef]
11. Wen, L.; Li, X.Y.; Gao, L.; Zhang, Y.Y. A New Convolutional Neural Network-Based Data-Driven Fault Diagnosis Method. *IEEE Trans. Ind. Electron.* **2018**, *65*, 5990–5998. [CrossRef]
12. Li, J.; Liu, Y.B.; Li, Q.J. Intelligent fault diagnosis of rolling bearings under imbalanced data conditions using attention-based deep learning method. *Measurement* **2022**, *189*, 110500. [CrossRef]
13. Gao, S.Z.; Xu, L.T.; Zhang, Y.M.; Pei, Z.M. Rolling bearing fault diagnosis based on SSA optimized self-adaptive DBN. *Isa Trans.* **2022**, *128*, 485–502. [CrossRef] [PubMed]

14. Vos, K.; Peng, Z.X.; Jenkins, C.; Shahriar, M.R.; Borghesani, P.; Wang, W.Y. Vibration-based anomaly detection using LSTM/SVM approaches. *Mech. Syst. Signal Process.* **2022**, *169*, 108752. [CrossRef]
15. Ayas, S.; Ayas, M.S. A novel bearing fault diagnosis method using deep residual learning network. *Multimed. Tools Appl.* **2022**, *81*, 22407–22423. [CrossRef]
16. Shao, H.D.; Xia, M.; Wan, J.F.; de Silva, C.W. Modified Stacked Autoencoder Using Adaptive Morlet Wavelet for Intelligent Fault Diagnosis of Rotating Machinery. *IEEE-Asme Trans. Mechatron.* **2022**, *27*, 24–33. [CrossRef]
17. Zhou, J.B.; Xiao, M.H.; Niu, Y.; Ji, G.J. Rolling Bearing Fault Diagnosis Based on WGWOA-VMD-SVM. *Sensors* **2022**, *22*, 6281. [CrossRef] [PubMed]
18. Chen, C.L.P.; Liu, Z.L. Broad Learning System: An Effective and Efficient Incremental Learning System Without the Need for Deep Architecture. *IEEE Trans. Neural Netw. Learn. Syst.* **2018**, *29*, 10–24. [CrossRef]
19. Wang, J.D.; Yang, Y.; Li, N. Randomization-based neural networks for image-based wind turbine fault diagnosis. *Eng. Appl. Artif. Intell.* **2023**, *121*, 106028. [CrossRef]
20. Wang, X.J.; Hua, T.; Xu, S.; Zhao, X.B. A Novel Rolling Bearing Fault Diagnosis Method Based on BLS and CNN with Attention Mechanism. *Machines* **2023**, *11*, 279. [CrossRef]
21. Fu, Y.; Cao, H.R.; Xuefeng, C.; Ding, J. Task-incremental broad learning system for multi-component intelligent fault diagnosis of machinery. *Knowl.-Based Syst.* **2022**, *246*, 108730. [CrossRef]
22. Yang, L.; Yang, Z.L.; Song, S.J.; Li, F.; Chen, C.L.P. Twin Broad Learning System for Fault Diagnosis of Rotating Machinery. *IEEE Trans. Instrum. Meas.* **2023**, *72*, 3510712. [CrossRef]
23. Zhou, J.M.; Liu, L.L.; Shen, X.W. SSDStacked-BLS with Extended Depth and Width: Infrared Fault Diagnosis of Rolling Bearings under Dual Feature Selection. *Mathematics* **2023**, *11*, 3677. [CrossRef]
24. Wang, X.J.; Wang, C.J.; Zhu, K.Y.; Zhao, X.B. A Mechanical Equipment Fault Diagnosis Model Based on TSK Fuzzy Broad Learning System. *Symmetry* **2023**, *15*, 83. [CrossRef]
25. Wu, T.T.; Zhuang, Y.F.; Fan, B.; Guo, H.N.; Fan, W.; Yi, C.; Xu, K.K. Multidomain Feature Fusion for Varying Speed Bearing Diagnosis Using Broad Learning System. *Shock Vib.* **2021**, *2021*, 6627305. [CrossRef]
26. Lu, J.T.; Cui, R.Q.; Li, S.M. An imbalanced sample intelligent fault diagnosis method using data enhancement and improved broad learning system. *Meas. Sci. Technol.* **2023**, *34*, 075106. [CrossRef]
27. Zhang, S.M.; Liu, Z.L.; Chen, C.L.P. Broad learning system based on the quantized minimum error entropy criterion. *Sci. China-Inf. Sci.* **2022**, *65*, 222203. [CrossRef]
28. Zhu, X.Q.; Qiu, T.; Qu, W.Y.; Zhou, X.B.; Atiquzzaman, M.; Wu, D.O. BLS-Location: A Wireless Fingerprint Localization Algorithm Based on Broad Learning. *IEEE Trans. Mob. Comput.* **2023**, *22*, 115–128. [CrossRef]
29. Feng, S.; Chen, C.L.P. Fuzzy Broad Learning System: A Novel Neuro-Fuzzy Model for Regression and Classification. *IEEE Trans. Cybern.* **2020**, *50*, 414–424. [CrossRef]
30. Liu, J.Q.; Wen, T.; Xie, G.; Cao, Y. Modified multi-scale symbolic dynamic entropy and fuzzy broad learning-based fast fault diagnosis of railway point machines. *Transp. Saf. Environ.* **2023**, *5*, tdac065. [CrossRef]
31. Felix, L.O.; Martins, D.; Monteiro, U.; Castro, B.M.; Pinto, L.A.V.; Martins, C.A.O. A Feature Selection Committee Method Using Empirical Mode Decomposition for Multiple Fault Classification in a Wind Turbine Gearbox. *J. Nondestruct. Eval.* **2023**, *42*, 85. [CrossRef]
32. Wang, J.W.; Niu, W.Q.; Yang, Y.H. Wind turbine output power prediction by a segmented multivariate polynomial-XGBoost model. *Energy Sources Part A—Recovery Util. Environ. Eff.* **2024**, *46*, 505–521. [CrossRef]
33. Yadav, S.; Patel, R.K.; Singh, V.P. Multiclass Fault Classification of an Induction Motor Bearing Vibration Data Using Wavelet Packet Transform Features and Artificial Intelligence. *J. Vib. Eng. Technol.* **2022**, *11*, 3093–3108. [CrossRef]